Structural Durability & Health Monitoring

Tech Science Press

https://doi.org/10.32604/sdhm.2026.079234

ARTICLE

Low-Frequency Ultrasonic Array Imaging of Interlayer Voids Hidden in Ballastless Track Structure of High-Speed Railway

Guopeng Fan[1,*], Xuefeng Chen[1], Hao Liu[1] and Jiaqing Zheng[2]

[1]School of Urban Railway Transportation, Shanghai University of Engineering Science, Shanghai, China
[2]Ottawa-Carleton Institute of Civil Engineering, University of Ottawa, Ottawa, ON, Canada

*Corresponding Author: Guopeng Fan. Email: phdfanry@sues.edu.cn

Received: 17 January 2026; Accepted: 30 March 2026; Published: 30 June 2026

ABSTRACT: Low-frequency ultrasonic array is commonly used to detect interlayer voids located in high-speed railway ballastless track, which is a typical multilayer concrete bonded structure. The difficulty of detection lies in the fact that the total focusing method (TFM) based on a single fixed sound velocity model cannot adapt to the acoustic propagation characteristics of multilayer structures, which is prone to generating artifacts. In addition, the long duration of low-frequency ultrasonic pulses is prone to causing significant deviations in defect localization. To address these issues, a theoretical model of the layered bonded structure is proposed. The acoustic wave propagation path and travel time calculation are clarified after combining the *Fermat's principle* and *Snell's law*, and the shortest path ray tracing (SPRT) is proposed, which achieves visual imaging of interlayer voids; The pulse peak delay (PPD) is applied to correct the travel time of low-frequency ultrasonic waves, and the shortest path ray tracing combined with pulse peak delay (PSPRT) is proposed, which significantly improves the localization accuracy of defects. Finally, by integrating the amplitude and phase information of scattered signals, the shortest path ray tracing based on pulse peak delay and sign coherence factor (PPSPRT) is constructed, which significantly enhances the SNR. The test results show that, compared with the conventional TFM, the proposed PPSPRT achieves average SNR improvements of 6.62 dB in numerical simulations and 14.30 dB in field tests, and reduces the average depth localization error of interlayer voids to merely 23.49% and 10.38% of that of TFM under corresponding test conditions, respectively. PPSPRT can provide important guidance for accurate imaging of interlayer voids.

KEYWORDS: Low-frequency ultrasonic array; interlayer voids; bonded structure; ray tracing; localization accuracy

1 Introduction

High-speed railways serve as the backbone of modern transportation systems, significantly enhancing the efficiency of passenger travel. These systems utilize a multilayer concrete bonding structure composed of track slabs, Cement Asphalt (CA) mortar layer, and base slab [1–4]. During the long-term service of high-speed railways, temperature differentials between the upper and lower surfaces of the track slabs can cause warping and deformation. Additionally, the cyclic loads imposed by trains can induce fatigue damage at the bonding interface between the track slabs and the CA mortar layer, leading to voids at the edges. This results in stress concentration, which adversely affects track smoothness, in severe cases, causing track slab fractures, potentially leading to derailment accidents that threaten both operational safety and the lives and property of the public [5–9]. Therefore, establishing a precise and efficient defect detection system for ballastless track structures is a critical technological requirement for ensuring the quality and operational safety of railway engineering.

Ultrasonic testing is a crucial nondestructive evaluation technique [10–13]. By analyzing the alterations in reflected, refracted, and other ultrasonic signals resulting from interactions with flaws during wave propagation through a medium, this technique can effectively determine the precise location and morphology of internal defects. It thereby enables the evaluation of the internal condition of structures [14–16]. Due to the significant attenuation of ultrasound within concrete, low-frequency ultrasound (below 100 kHz) is commonly employed in structural health monitoring applications [17,18].

As the materials used in engineering structures become increasingly complex, concrete structures are no longer composed of a single medium. This shift has driven the advancement of ultrasonic nondestructive testing (NDT) technology from focusing on single-layer homogeneous media to adapting to intricate multilayer systems, consequently evolving the core technical challenges associated with it. For single-layer concrete, the focus of research has been on enhancing imaging contrast and the detection capability for complex defects. Yang et al. [19] proposed a diffusion attenuation compensation-based solid directional correction method (DAC-SDCM) by studying the diffusion attenuation compensation factor and the solid directional correction factor, significantly improving the identification of blind-spot defects within concrete structures. Zhang et al. [20] introduced an abnormal pathway imaging method based on average ultrasonic velocity, combining with a time of flight (TOF) optimization technique based on noise anomalies, yielding imaging results superior to traditional tomographic imaging. This approach provides a feasible solution for high-quality ultrasonic imaging and low-cost field assessment. Zhan et al. [21] developed a three-dimensional imaging technique based on diffused ultrasound, successfully enabling simultaneous and precise detection of the number, location, and depth of multiple internal cracks in concrete structures. Yang et al. [22] addressed the inconsistencies in wave focus caused by multiple scattering during crack detection in concrete by constructing a novel imaging function, resulting in an improved high-resolution time-reversal imaging method that significantly enhances imaging accuracy for various types of cracks. Baek et al. [23] tackled the limitations of traditional detection methods for reinforced concrete, which struggle with penetrating dense bar and are prone to imaging artifacts and low resolution. They proposed null subtraction imaging (NSI) technology, which significantly enhances the contrast and resolution of images depicting the internal structure of concrete.

The aforementioned methods perform exceptionally well in detecting single-layer concrete structures; however, when applied to multilayer structures such as ballastless track systems, they do not adequately consider interface refraction and variations in sound speed. This often leads to distortion in defect localization and blurred imaging [24]. Consequently, researchers have explored imaging algorithms specifically designed for multilayer structures. To address the challenges of acoustic wave refraction and velocity variation in multi-layer detection, Zhang et al. [25] developed a multi-mode TFM framework integrating ray theory, which extended the traditional TFM proposed by Holmes et al. [26], thereby establishing a comprehensive solution for multilayer imaging. On this basis, Budyn et al. [27] further refined ray-based refraction modeling for multilayer interfaces, developed a fast full-area detection sensitivity evaluation method for multilayer media, and realized accurate prediction of small-defect multi-view imaging response, providing an efficient quantitative tool for multilayer imaging scheme optimization. This series of theoretical foundations has inspired concrete-specific multilayer imaging methods. Wu et al. [28] proposed a two-step detection method based on array ultrasonics and deep learning, which integrates array SAFT imaging with intelligent image recognition. This approach not only applies to single-layer concrete defect detection but is also suitable for multilayer concrete structures like tunnel secondary linings. However, the diversity and scale of the model training data are limited, and its generalization ability in complex real-world environments still requires enhancement. Lin et al. [29] combined synthetic aperture focusing technology (SAFT) with multilayer delayed acoustic summation (MLDAS) to propose an ultrasonic data analysis method tailored

to multilayer concrete structures, thereby improving imaging quality and defect localization precision. Zhu et al. [30] introduced a time-domain topological energy (TDTE) imaging method based on Lamb waves to address the issue of void defects in multilayer concrete, achieving high-precision localization of voids while minimizing imaging artifacts. Li et al. [31] integrated forward ray tracing and synthetic aperture focusing technique (RF-SAFT) ultrasound imaging technique, which, compared to traditional reverse ray tracing synthetic aperture focusing technology (RR-SAFT), reduced computational time by 70% and also demonstrated superior imaging accuracy compared to the root mean square RMS-SAFT, significantly enhancing computational efficiency while maintaining precision. Si et al. [32] proposed a fast multilayer ray tracing (FMRT) method that combines *Snell's law* and *Fermat's principle*, capable of efficiently and qualitatively distinguishing three bonding states between tunnel linings and surrounding rock. Despite these advancements in multilayer concrete structure detection, there remains a need to further refine the quantitative analysis capabilities regarding defect morphology and size.

This paper addresses the challenge of rapidly and accurately detecting defects in multilayer concrete structures by proposing a shortest-path ray tracing imaging method based on pulse delay symbol coherence, aimed at significantly improving the efficiency and image signal-to-noise ratio (SNR). The main contributions are as follows:

(1) A shortest path ray trajectory tracing (SPRT) method is constructed by incorporating *Snell's law* to constrain the refraction point position. Compared with the minimum travel-time ray tracing (MTRT) method, which realizes visual imaging of interlayer voids by selecting the shortest travel-time path as the actual ultrasonic propagation path, the proposed SPRT markedly improves the imaging efficiency of interlayer voids.
(2) The shortest path ray tracing combined with pulse peak delay (PSPRT) method is proposed by using a peak pulse delay (PPD) factor to correct the traveling time for low-frequency ultrasound. The PSPRT markedly improves the localization accuracy of interlayer voids.
(3) The sign coherence factor (SCF) is extracted from the received signal and utilized as phase information, resulting in the construction of shortest path ray tracing based on pulse peak delay and sign coherence factor (PPSPRT) method, which effectively suppresses artifacts in ultrasonic images.

The remainder of this paper is organized as follows: Section 2 details on the imaging principles of TFM, MTRT, SPRT, PSPRT, and PPSPRT. Section 3 presents a simulation study on void defects. Section 4 describes experimental investigations of void defects. Section 5 quantitatively evaluates imaging performance in terms of SNR, defect length, and depth. Finally, Section 6 summarizes the primary contributions and outlines future research directions.

2 Methodology

2.1 TFM

The acquisition of abundant and effective signals by the ultrasound array is crucial for accurate imaging. The flowchart for collecting full matrix data using a linear array with an element count of N is illustrated in Fig. 1. Each element in the array is sequentially excited to emit ultrasound signals, while all N elements simultaneously receive the reflected signals during each pulse, resulting in N sets of signals as shown in Fig. 1a,b. This process continues until the reflected ultrasound signals emitted by the N-th element are fully received, leading to a total of $N \times N$ sets of ultrasound signals being gathered, thus completing the acquisition of full matrix data, as depicted in Fig. 1c.

The principle of the full focusing method is based on the time-domain signal's delay-and-sum technique. It focuses the acquired scattered signals at a specific grid point in the area being inspected, subsequently

performing point-by-point focusing within the test region [26,33–35]. To calculate the total distance from the focus point to the excitation and receiving elements, the ratio of this distance to the speed of sound of ultrasound in the inspected sample is utilized to determine the travel time of the acoustic wave from the element to the focal point and back to the element, as described in Eq. (1).

$$\tau_{ij}(x,z) = \frac{\sqrt{(x-x_i)^2+(z-z_i)^2}+\sqrt{(x-x_j)^2+(z-z_j)^2}}{c} \tag{1}$$

where (x,z) represents the coordinates of the focal point, τ_{ij} is the travel time of the acoustic wave, the subscript i denotes the transmitting element, j denotes the receiving element, and c represents the propagation speed of the ultrasound in the inspected sample.

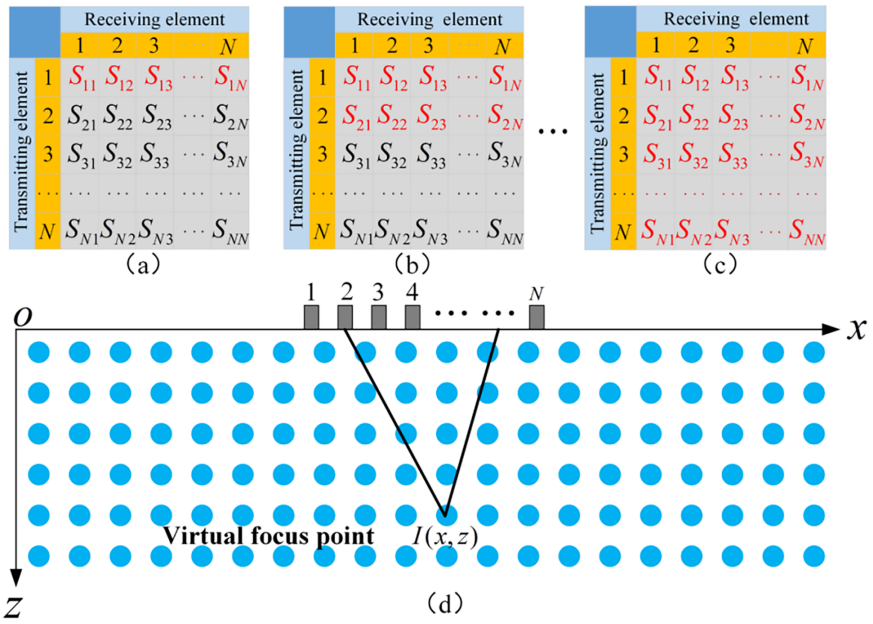

Figure 1: Schematic diagram of full matrix capture: (**a**) Element 1 is excited while all elements receive; (**b**) Element 2 is excited while all elements receive; (**c**) Element N is excited while all elements receive; (**d**) Virtual focusing.

After calculating the travel time, the corresponding amplitudes of all echo signals are summed, allowing the amplitude at any target focal point $I_{TFM}(x,z)$ within the inspected sample to be expressed as:

$$I_{TFM}(x,z) = \frac{1}{N^2}\sum_{i=1}^{N}\sum_{j=1}^{N} S_{ij}\left(\tau_{ij}(x,z)\right) \tag{2}$$

where $I_{TFM}(x,z)$ represents the pixel value, N denotes the number of array elements, and S_{ij} is the scattered signal transmitted by the i-th array element and received by the j-th array element.

2.2 MTRT

The MTRT imaging method is based on *Fermat's principle*, which asserts that waves always propagate along the path that requires the least travel time, corresponding to their actual physical propagation path. This method utilizes ray tracing algorithms from computer graphics to simulate the propagation of ultrasound through multilayered media structures. It accounts for refraction at different material interfaces, exhaustively searching all possible refraction point locations. By calculating the total acoustic propagation time for each

path and selecting the one with the shortest duration as the actual propagation path, high-precision imaging and detection of internal defects within multilayer structures can be accurately achieved.

The schematic diagram illustrating the solution for the acoustic propagation path within multilayer structures based on the MTRT method is shown in Fig. 2. The steps involved in implementing MTRT are as follows: First, the region to be imaged is divided into several discrete grid points, and an excitation point $A\left(x_A, z_A\right)$ is then determined. Next, the interface between the first and second layers is discretized into m incidence points $\left(P_1, P_{2,\ldots,} P_m\right)$, while the interface between the second and third layers is discretized into m incidence points $\left(Q_1, Q_{2,\ldots,} Q_m\right)$. The refraction points are fully explored to obtain the shortest propagation distance. The travel time of the acoustic wave is calculated based on this distance. Thus, the distances between the transducer and the arbitrary imaging point, denoted as r_{AP}, r_{PQ} and r_{QD} can be expressed as:

$$r_{AP} = \sqrt{\left(x_P - x_A\right)^2 + d_1} \tag{3}$$

$$r_{PQ} = \sqrt{\left(x_P - x_Q\right)^2 + d_2} \tag{4}$$

$$r_{QD} = \sqrt{\left(x_Q - x_D\right)^2 + \left(z_D - d_1 - d_2\right)^2} \tag{5}$$

where r_{AP} represents the distance from the emission point A to the first refractive point. r_{PQ} represents the distance between the first refraction point and the second refraction point. r_{QD} represents the distance between the second refraction point and the grid point within the third layer of the medium; d_1, d_2, and d_3 are the thicknesses of each medium layer.

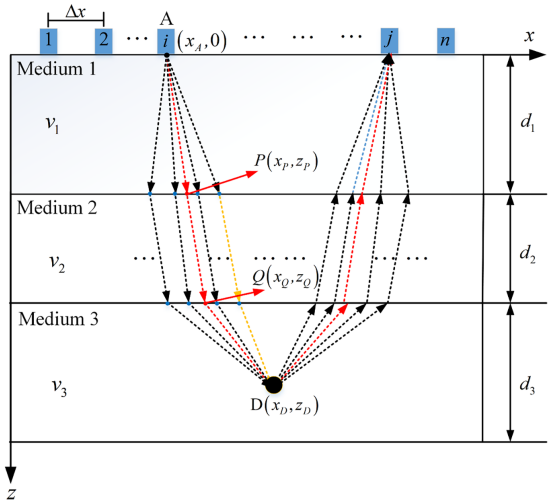

Figure 2: Schematic diagram of solving sound propagation path in multilayer structure based on MTRT.

In MTRT, the minimum propagation time T_{ijMTRT} is determined among all refraction paths, adhering to *Fermat's principle*. Subsequently, the pixel intensity at the spatial grid points can be calculated by substituting the travel time with T_{ijMTRT}.

$$T_{ijMTRT} = \frac{r_{AP}}{v_1} + \frac{r_{PQ}}{v_2} + \frac{r_{QD}}{v_3} \tag{6}$$

$$T_{ijMTRT} = \min\left[T_{iMTRT} + T_{jMTRT}\right], i, j = 1, 2, \cdots, N \tag{7}$$

$$I_{MTRT}\left(x, z\right) = \frac{1}{N^2}\sum_{i=1}^{N}\sum_{j=1}^{N} S_{ij}\left(T_{ijMTRT}\left(x, z\right)\right) \tag{8}$$

where v_1, v_2, and v_3 are the sound velocities in medium 1, medium 2, and medium 3, respectively; T_{iMTRT} and T_{jMTRT} represent the propagation times during the emission and reception processes, respectively.

2.3 SPRT

For ultrasonic imaging in multi-layer media, the FMRT method proposed by Si et al. [32] is developed based on the MTRT method, and constrains the traversal range of refraction points on a single interface in combination with Snell's Law. However, this method is established on a two-layer single-interface medium model. When extended to a three-layer dual-interface structure, it still requires full combination traversal of the refraction points on both interfaces, which will lead to a significant increase in computation time. To address this limitation, this paper proposes a SPRT algorithm suitable for three-layer dual-interface media. Through a linked constraint mechanism for refraction points on dual interfaces, the proposed algorithm achieves fast and accurate solution of ray paths in multi-layer structures, and further improves imaging efficiency. This method aims to facilitate the efficient determination of acoustic propagation paths in multi-layer media. According to *Snell's Law*:

$$\theta = \arcsin\left(\frac{v_2 \sin\alpha}{v_1}\right) \tag{9}$$

where α represents the angle of incidence, θ denotes the angle of refraction, v_1 is the sound velocity before refraction, and v_2 is the sound velocity after refraction.

The schematic diagram for solving acoustic propagation paths within multilayer structures based on the SPRT method is depicted in Fig. 3. The implementation steps of SPRT are as follows: we adopt the same grid division approach used in MTRT to determine the coordinates of the excitation source and the spatial positions of each imaging grid point. For illustrative purposes, we begin with the case where the grid point is located to the right of the excitation source. When the grid point is positioned to the left of the excitation source, the processing logic follows a similar pattern as that on the right side, and thus will not be elaborated further.

(1) If the grid point is located within the first layer of the medium, imaging of the area to be inspected can be achieved by following the TFM.

(2) If the grid point is located within the second layer of the medium: The refraction point P_r between the first and second layers resides along the segment MN, and this refraction point P_r moves horizontally by one grid interval towards m from N at each iteration. As P_r moves, the endpoint of the refraction path also shifts horizontally to the right, gradually approaching the target grid point $D_r\,(x_r, z)$. Because the imaging region has been discretized into grids, there will be a slight horizontal position deviation between this endpoint and the target grid point; the denser the grid division, the smaller this deviation becomes. Therefore, we set a positional deviation threshold $|x_r - x| \le \varepsilon$. When point P_r moves to point P and meets the condition of this threshold, the movement is stopped. We then compute the time T_{APD} required for the acoustic wave to propagate along the refracted path $A \to P \to D$.

$$\begin{aligned} T_{iSPRT} &= T_{APD} \\ &= \frac{\|AP\|}{v_1} + \frac{\|PD\|}{v_2} \\ &= \frac{\sqrt{(x_P - x_A)^2 + {d_1}^2}}{v_1} + \frac{\sqrt{(x - x_P)^2 + (z - d_1)^2}}{v_2} \end{aligned} \tag{10}$$

where x_r must satisfy the following conditions:

$$\begin{cases} \sin(\alpha) = \dfrac{\|MP\|}{\|AP\|} = \dfrac{|x_A - x_P|}{\sqrt{(x_A - x_P)^2 + {d_1}^2}} \\ \theta = \arcsin\left(\dfrac{v_2 \sin(\alpha)}{v_1}\right) \\ \Delta_{d_1} = z - d_1 \\ symb = \begin{cases} 1, & x > x_A \\ -1, & x < x_A \end{cases} \\ x_r = x_{P_r} + symb \cdot \Delta_{d_1} \tan(\theta) \\ |x_r - x| \le \varepsilon \end{cases} \tag{11}$$

(3) If the grid point is located within the third layer of the medium: At this stage, the refraction point P_r between the first and second layers resides along the segment MN. According to *Snell's law*, the corresponding refraction point Q_r between the second and third layers can be found along the segment JH. The point P_r moves horizontally from point m towards point N in increments of one grid interval, while the point Q_r moves synchronously from point J towards point H. During this process, the endpoint of the refraction path $D_r(x_r, z)$ gradually approaches the target grid point $D(x, z)$. When the point P_r reaches point P and the point Q_r corresponds to the position Q, if the pre-set threshold condition $|x_r - x| \le \varepsilon$ is met, the movement is halted. The time T_{APQD} required for the acoustic wave to propagate along the refracted path $A \to P \to Q \to D$ is then calculated.

$$\begin{aligned} T_{iSPRT} = T_{APQD} &= \frac{\|AP\|}{v_1} + \frac{\|PQ\|}{v_2} + \frac{\|QD\|}{v_3} \\ &= \frac{\sqrt{(x_P - x_A)^2 + {d_1}^2}}{v_1} + \frac{\sqrt{(x_Q - x_P)^2 + {d_2}^2}}{v_2} \\ &\quad + \frac{\sqrt{(x - x_Q)^2 + (z - d_1 - d_2)^2}}{v_3} \end{aligned} \tag{12}$$

where x_r and x_{Q_r} must satisfy the following conditions:

$$\begin{cases} \sin\alpha = \dfrac{\|MP_r\|}{\|AP_r\|} = \dfrac{|x_A - x_P|}{\sqrt{(x_A - x_P)^2 + {d_1}^2}} \\ \sin\theta = \dfrac{\|WQ_r\|}{\|PQ_r\|} = \dfrac{|x_Q - x_P|}{\sqrt{(x_Q - x_P)^2 + (d_1 + d_2)^2}} \\ \theta = \arcsin\left(\dfrac{v_2 \sin\alpha}{v_1}\right) \\ \beta = \arcsin\left(\dfrac{v_3 \sin\theta}{v_2}\right) \\ symb = \begin{cases} 1, & \text{if} \quad x > x_A \\ -1, & \text{if} \quad x < x_A \end{cases} \\ x_{Q_r} = x_{P_r} + symb \cdot d_2 \tan(\theta) \\ x_r = x_{Q_r} + symb \cdot \Delta_{d2} \tan(\beta) = x_{Q_r} + symb \cdot (z - d_1 - d_2) \tan(\beta) \\ |x_r - x| \le \varepsilon \end{cases} \tag{13}$$

The pixel values of spatial grid points under the shortest path ray tracing method can be expressed as:

$$I_{SPRT}(x,z) = \frac{1}{N^2}\sum_{i=1}^{N}\sum_{j=1}^{N} S_{ij}\left(T_{ijSPRT}(x,z)\right) \tag{14}$$

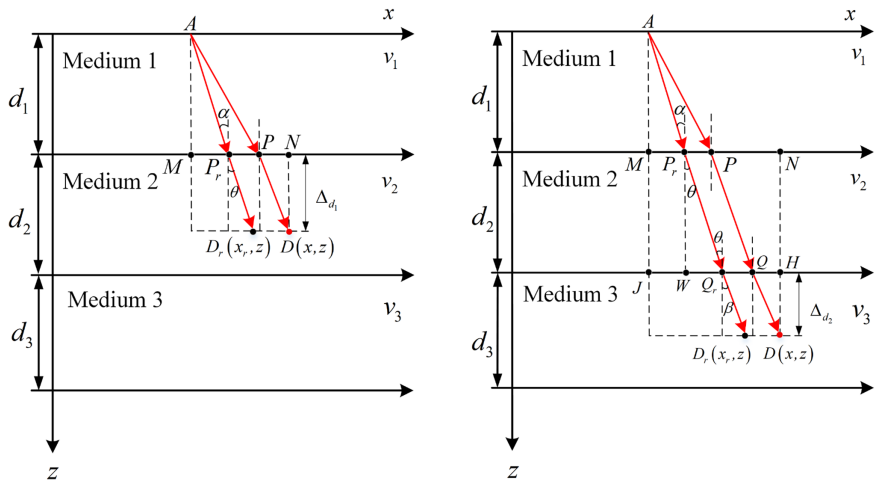

Figure 3: Schematic diagram of the acoustic propagation path calculation within a multilayer structure based on SPRT.

2.4 PSPRT

The arrival time of the wavefront in low-frequency ultrasound long pulse signals exhibits a fixed time offset relative to the peak of the echo signal's Hilbert envelope. Traditional imaging methods calculate travel time based on the wavefront arrival time. However, the actual effective energy of the echo is concentrated at the envelope peak. Low-frequency signals with longer pulse durations are subject to image position deviations, resulting in localization errors. Therefore, in the image reconstruction algorithm, it is essential to correct the acoustic travel time by incorporating a pulse peak delay term *PPD*, thereby enhancing the accuracy of defect imaging localization. A schematic representation of the *PPD* is illustrated in Fig. 4. The SPRT imaging formula, corrected for the pulse peak delay, is as follows:

$$I_{PSPRT}(x,z) = \frac{1}{N^2}\sum_{i=1}^{N}\sum_{j=1}^{N} S_{ij}\left(T_{ijSPRT}(x,z) + PPD\right) \tag{15}$$

where *PPD* is defined as the time delay between the wavefront arrival and the peak of the Hilbert envelope.

2.5 PPSPRT

The TFM primarily relies on the amplitude information of echo signals for imaging, while the phase information is underutilized, resulting in numerous artifacts in the imaging. To address this issue, this study extracts phase information from the full matrix data to construct a SCF. Based on this, a weighted operation is performed on the scattered signals from the defects, thereby developing the SCF imaging method. The detailed process is as follows:

A special phase quantization method is employed to divide the interval of $[-\pi, \pi]$ into two smaller sub-intervals, labeled as $\left(-\frac{\pi}{2}, \frac{\pi}{2}\right]$ and $\left[-\pi, -\frac{\pi}{2}\right] \cup \left(\frac{\pi}{2}, \pi\right]$. When the phases of two echo signals fall within the same sub-interval, they can be considered to have the same polarity. Useful information can be represented solely using the symbol bit b_i:

$$b_i(t) = \begin{cases} -1, & \text{if} \quad S_i(t) < 0 \\ 1, & \text{if} \quad S_i(t) \geq 0 \end{cases} \tag{16}$$

where S_i represents the i-th scattered signal. Due to $\sum b_i^2 = N$, the variances of b_i as follows:

$$\sigma^2 = \frac{N\sum_{i=1}^{N} b_i^2 - \left(\sum_{i=1}^{N} b_i\right)^2}{N^2} = 1 - \left(\frac{1}{N}\sum_{i=1}^{N} b_i\right)^2 \tag{17}$$

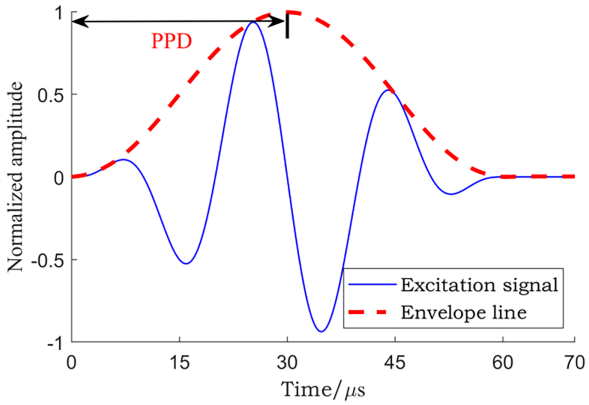

Figure 4: Schematic diagram of pulse peak delay.

The variance σ^2 can be calculated from the average of the symbols of the echo signals, with σ^2 distributed between 0 and 1. The computation method for the SCF is presented in Eq. (18). When the symbols of the aperture data are all consistent, the SCF reaches its maximum value of 1; conversely, when the symbols are evenly distributed between positive and negative, the SCF attains its minimum value of 0. Since the SCF only considers the polarity of the aperture data, it is straightforward to implement.

$$\mathrm{SCF}_i = 1 - \sqrt{1 - \left[\frac{1}{N}\sum_{j=1}^{N} b_{ij}\left(T_{ijPSPRT}(x,z)\right)\right]^2} \tag{18}$$

$$b_{ij}(t) = \begin{cases} -1, & \text{if} \quad S_{ij}(t) < 0 \\ 1, & \text{if} \quad S_{ij}(t) \geq 0 \end{cases} \tag{19}$$

$$T_{ijPSPRT} = T_{ijSPRT} + PPD, i, j = 1, 2, \cdots, N \tag{20}$$

where $T_{ijPSPRT}$ represents the travel time with the added peak delay factor.

The PPSPRT imaging Eq. (21) is as follows:

$$I_{PPSPRT}(x,z) = \frac{1}{N}\sum_{i=1}^{N}\left[\mathrm{SCF}_i \cdot \left(\frac{1}{N}\sum_{j=1}^{N} S_{ij}\left(T_{ijPSPRT}(x,z)\right)\right)\right] \tag{21}$$

3 Simulation

3.1 Finite Element Modeling

A two-dimensional finite element simulation model of a multilayer ballastless track structure was established using COMSOL Multiphysics 6.3. Numerical simulations were conducted on the ballastless track model containing defects with various void lengths. Fig. 5 illustrates the schematic of two-dimensional finite element simulations for both a healthy ballastless track and ballastless tracks with different void-length defects. The model consists of a base plate, a cement asphalt (CA) mortar layer, and a track slab. Twelve sensors were arranged on the surface of the model, with a center-to-center spacing of 30 mm between the sensors. Four different lengths of void regions were set within CA mortar layer, specifically: 300 mm × 15 mm, 250 mm × 15 mm, 200 mm × 15 mm, and 150 mm × 15 mm. The material parameters for each layer are shown in Table 1.

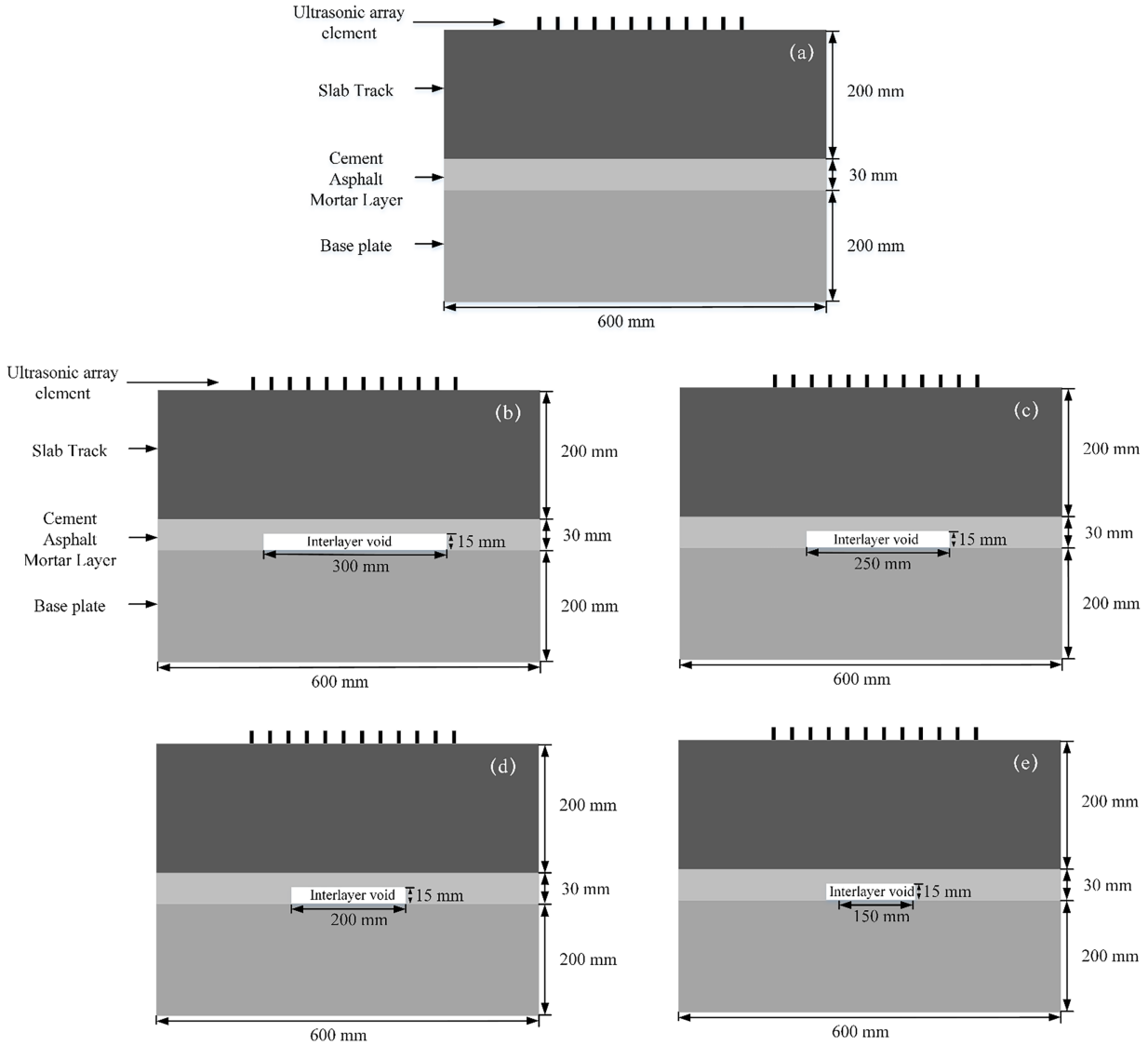

Figure 5: Simulation diagram of ballastless track structure: (**a**) healthy ballastless track; (**b**) 300 mm × 15 mm void defect; (**c**) 250 mm × 15 mm void defect; (**d**) 200 mm × 15 mm void defect; (**e**) 150 mm × 15 mm void defect.

Table 1: Material parameters of each layer of ballastless track structure.

Material	Shear Wave Velocity (m/s)	Wavelength (mm)	Density (kg/m^3)	Poisson's Ratio	Elastic Modulus (MPa)
Slab track	2450	49	2500	0.2	36,500
CA mortar	1223	24	1800	0.2	7000
Base plate	2236	45	2500	0.2	31,500
Interlayer void	0	0	1.29	0	0

In this simulation, a 3-cycle Hanning-window-modulated pulse signal with a center frequency of 50 kHz was adopted as the excitation source. The corresponding time-domain waveform and frequency spectrum are presented in Fig. 6.

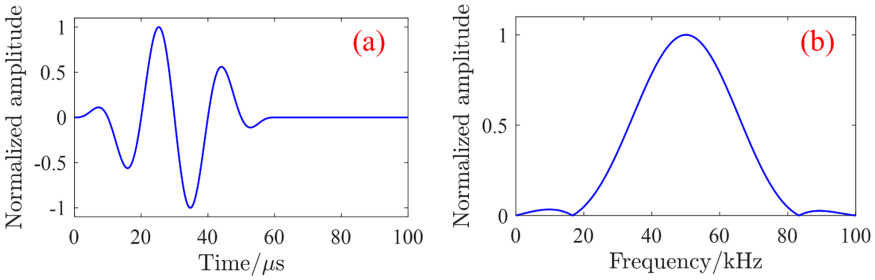

Figure 6: Excitation signal: (**a**) Time-domain waveform; (**b**) Frequency spectrum.

3.2 Sound Field Analysis

Through the finite element model of the multilayer ballastless track structure with void defects, the full matrix simulation data were obtained, and the results were analyzed to observe the transient acoustic field during the propagation of acoustic waves within the track slab structure. Using the 6th element as the excitation source, the acoustic field distributions at four specific time instances 60.3, 86.6, 104, and 128 μs are depicted in Fig. 7. In Fig. 7a, at 60.3 μs, the acoustic waves propagate within the first layer of the medium, accompanied by the emergence of surface waves. Fig. 7b shows the situation at 86.6 μs, where the acoustic waves reaches the upper surface of the intermediate layer, resulting in refraction, while the surface wave continues to travel along the surface of the first layer. In Fig. 7c, at 104 μs, when the acoustic wave propagates to the void defect, it undergoes both reflection and refraction. Finally, Fig. 7d illustrates that at 128 μs, the defect-reflected waves propagates to the upper surface of the first layer and is detected by the sensor.

Fig. 8a presents the signal waveforms captured by all 12 receiving channels with the first sensor acting as the transmitter. The obtained signals include both the surface waves and the scattered waves from the defects. The surface waves signal reflects the propagation of ultrasound in the defect-free region, while the scattered wave signal, caused by the void defects, characterizes the scattering behavior of ultrasound in the defective area. Fig. 8b demonstrates that by subtracting the full matrix data of the healthy plate from the corresponding full matrix data collected from the defective plate, the scattered wave signals induced by the void defects were successfully isolated.

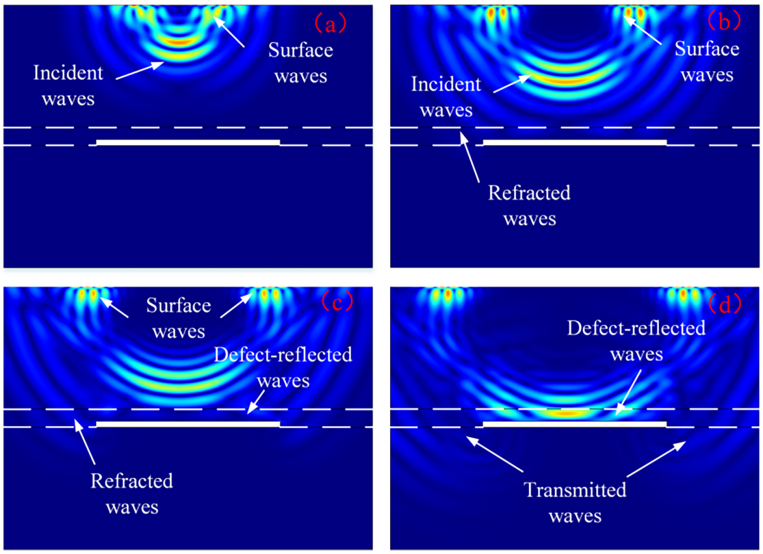

Figure 7: Transient sound field of ballastless track structure: (**a**) 60.3 μs; (**b**) 86.6 μs; (**c**) 104 μs; (**d**) 128 μs.

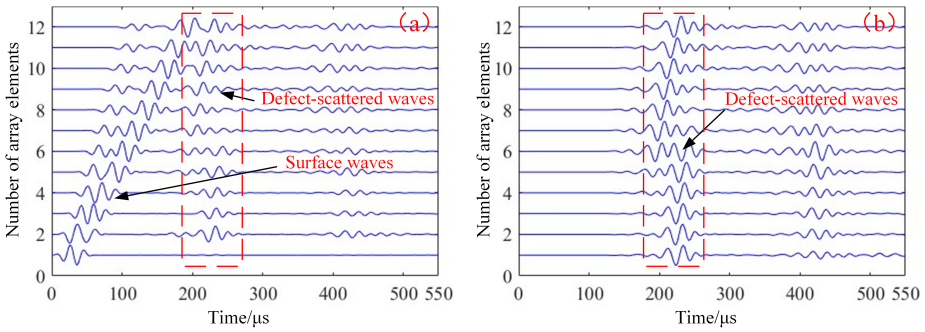

Figure 8: Signals emitted by the first sensor and received by 12 sensors: (**a**) Original signals; (**b**) Scattered signals.

3.3 Simulation Results

For the finite element model containing a void defect measuring 300 mm × 15 mm, detection was conducted sequentially using the MTRT and SPRT methods. The SNR is used to quantitatively evaluate the imaging quality, and the calculation Eq. (22) is:

$$SNR = 20\lg\left|\frac{I_{Max}}{I_{Average}}\right| \tag{22}$$

where I_{Max} and $I_{Average}$ represent the maximum pixel value and the average pixel value within the imaging area, respectively.

The imaging results and the required imaging times are illustrated in Fig. 9 and presented in Table 2, where the white box highlights the actual defect location. All data calculations and processing operations were implemented in MATLAB R2024a, using an AMD Ryzen 7 4800H CPU (with integrated Radeon Graphics) running at a main frequency of 2.90 GHz. It is clear that both SPRT and MTRT provide consistent imaging results; however, the time consumed by SPRT is only 20.762/28.103 = 0.739 times that of MTRT, indicating a 26.1% reduction in imaging time. This demonstrates that SPRT significantly enhances the

imaging efficiency for void defects in multilayer structures. Consequently, all subsequent void detection will be based on the SPRT method for further improvements.

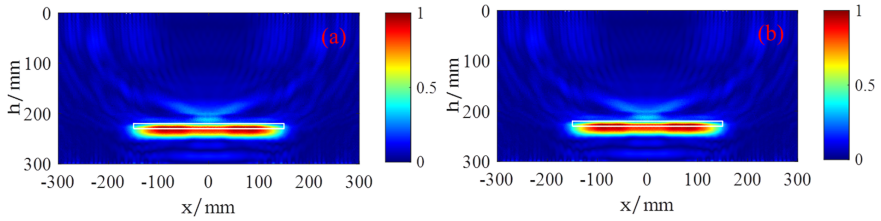

Figure 9: Ultrasonic imaging of void defects contained in the CRTS II ballastless track: (**a**) MTRT; (**b**) SPRT.

Table 2: Required imaging time of the MTRT and SPRT.

Method	Required Imaging Time (s)
MTRT	28.103
SPRT	20.762

Ultrasonic imaging was performed sequentially using four methods: TFM, SPRT, PSPRT, and PPSPRT, with the final results presented in Fig. 10a–d, respectively. The imaging results indicate that all four methods can accurately detect the presence of void defects within the ballastless track; however, significant differences are observed in terms of void length, depth, and image signal-to-noise ratio SNR. To further analyze the imaging performance of these four methods, intensity curves of the ultrasonic images were extracted, and the SNR was calculated to quantitatively assess the accuracy of defect localization and the effectiveness of noise suppression. The lateral intensity curve and the vertical intensity curve are shown in Fig. 11a,b, respectively. The lateral intensity curve reveals that the lateral ranges of the voids detected by TFM, SPRT, PSPRT, and PPSPRT are [−144.5, 144.5 mm], [−140.5, 140.5 mm], [−140, 140 mm], and [−139, 139 mm], respectively, resulting in void lengths of 289, 281, 280, and 278 mm. The actual length is 300 mm, and the length errors are 11, 19, 20, and 22 mm, respectively.

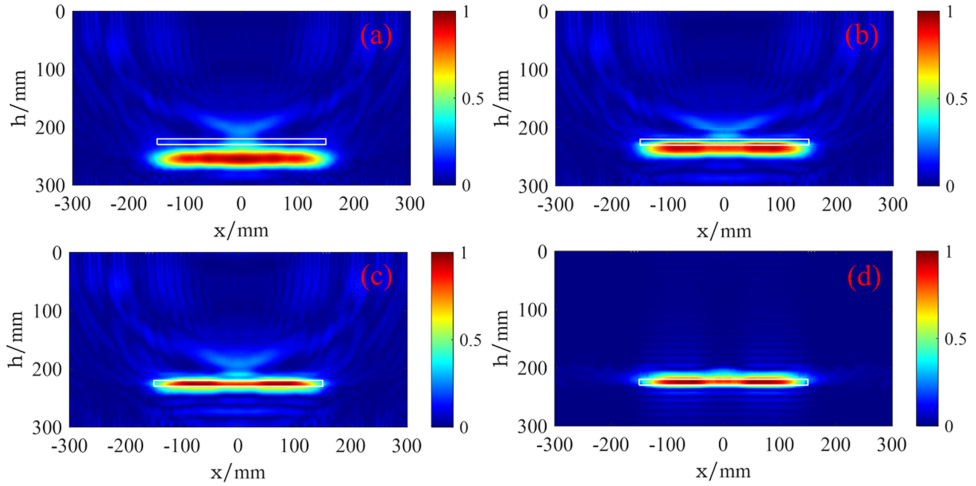

Figure 10: Numerical imaging results of different methods (the length of void is 300 mm): (**a**) TFM; (**b**) SPRT; (**c**) PSPRT; (**d**) PPSPRT.

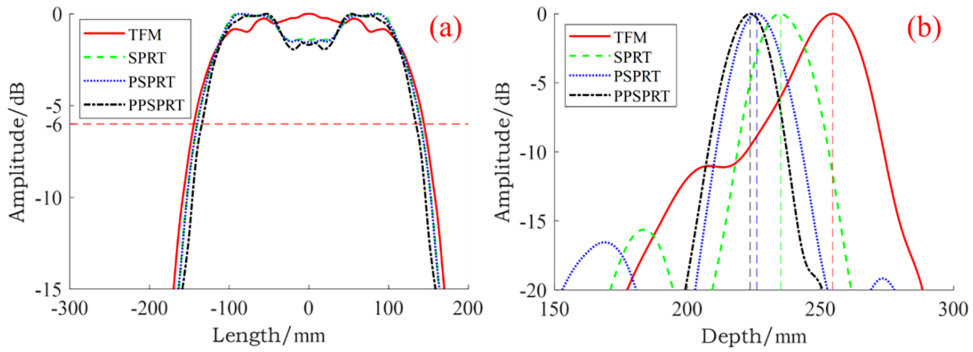

Figure 11: Numerical intensity curves of different methods (the length of void is 300 mm): (**a**) Transverse intensity curves; (**b**) Longitudinal intensity curves.

The vertical intensity curve indicates that the depths of the voids detected by TFM, SPRT, PSPRT, and PPSPRT are 254.5, 235, 227.5, and 224.5 mm, respectively. The actual depth is 215 mm, yielding depth errors of 39.5, 20, 12.5, and 9.5 mm, respectively. The SNRs of the ultrasonic images obtained using TFM, SPRT, PSPRT, and PPSPRT are 21.42, 22.14, 22.38, and 27.88 dB, respectively. The lengths, depths, and SNRs of the voids derived from the simulations are summarized in Table 3. The research findings demonstrate that in terms of void length detection, the performance of TFM, SPRT, PSPRT, and PPSPRT decreases successively, while in terms of void depth and SNR, the performance of TFM, SPRT, PSPRT, and PPSPRT improves sequentially. Notably, PPSPRT significantly outperforms the other methods in terms of depth localization and image SNR.

Table 3: The length, depth, and SNR of voids obtained from simulation.

Methods	SNR	Real Length	Detected Length	Length Error	Real Depth	Detected Depth	Depth Error
TFM	21.42 dB	300 mm	289 mm	11 mm	215 mm	254.5 mm	39.5 mm
SPRT	22.14 dB	300 mm	281 mm	19 mm	215 mm	235 mm	20 mm
PSPRT	22.38 dB	300 mm	280 mm	20 mm	215 mm	227.5 mm	12.5 mm
PPSPRT	27.88 dB	300 mm	278 mm	22 mm	215 mm	224.5 mm	9.5 mm

In summary, due to TFM's failure to account for the differences in sound speed between various media, the locations of void defects in the imaging results exhibit certain discrepancies, and the presence of excessive noise leads to comparatively poor imaging quality. In contrast, SPRT calculates the sound time more accurately by considering the acoustic wave speeds in different media, resulting in detected void defect locations that are closer to their actual positions, although some discrepancies remain and noise issues continue to be notable. PSPRT further adds a peak delay term to correct the sound time, allowing the detected defect locations to approach the actual positions; however, significant noise still persists in the images. When utilizing PPSPRT for defect detection, not only is the deviation of defect locations in the ultrasonic images minimal, but the noise in the images is also significantly reduced.

4 Experiment

4.1 Experimental Setup

The A1040 MIRA Concrete Tomography Ultrasonic Imager, produced by ACSYS, is capable of detecting internal defects in single-layer concrete structures, as illustrated in Fig. 12a. However, the imaging approach

employed by this instrument is based on a single uniform sound speed model, which is not suitable for detecting defects in multilayer bonded concrete structures. Therefore, this study only utilizes the instrument to collect ultrasonic echo signals, employing the imaging method developed in this paper for signal processing and defect detection using MATLAB R2024a. This instrument features a total of 48 Dry Point Contact (DPC) transducers arranged in a 4 by 12 array configuration, with specific parameters detailed in Table 4. During the transmission and reception of signals, the instrument adheres to the principle of acoustic reciprocity. The sampling frequency is set at 1 MHz, with the excitation signal's center frequency at 50 kHz. This is consistent with the signals used in the simulation. The corresponding time-domain waveform and frequency spectrum are shown in the Fig. 6. Utilizing a 50 kHz signal as the excitation frequency enhances the propagation distance of ultrasonic waves in concrete, reduces acoustic wave attenuation, and is beneficial for detecting defects located deeper within the material.

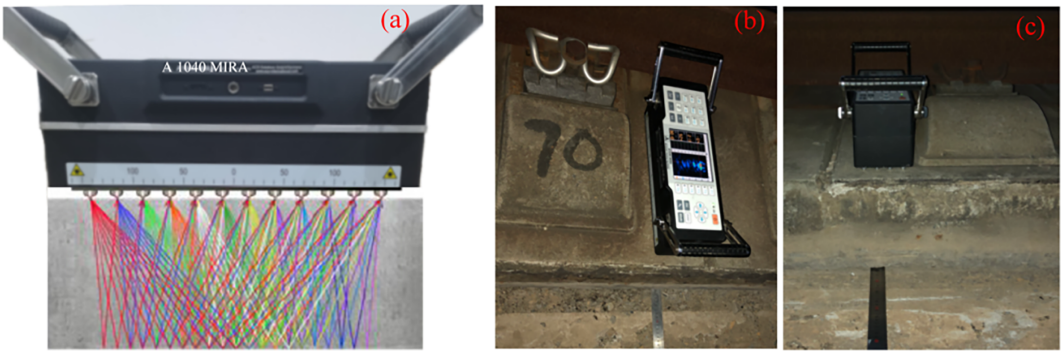

Figure 12: Experimental detection of void defects located at ballastless track structure: (**a**) A1040 MIRA concrete tomography ultrasound imager; (**b**) Case 1; (**c**) Case 2.

Table 4: Parameters of A1040 MIRA.

Parameters	Numerical Values
Type of contact between the element and the object being detected	Dry point contact (without the need for coupling agent)
Type of acoustic waves generated	Shear wave
Number of elements	12 rows × 4 per row = 48
Center spacing of adjacent elements (mm)	30
Center frequency of excitation signal (kHz)	50
Signal bandwidth (kHz)	20~80
Sampling frequency (kHz)	1000
Number of received signals	66
Shear wave velocity in the slab (m/s)	2450
Shear wave velocity in the CA mortar (m/s)	1223
Shear wave velocity in the base plate (m/s)	2236

To validate the imaging capabilities of the four methods—TFM, SPRT, PSPRT, and PPSPRT—ultrasonic imaging inspections were conducted on a ballastless track structure along a certain high-speed railway segment. The interlayer voids are located between the mortar layer and the base slab of the ballastless track. Case 1 and Case 2 are illustrated in Fig. 12b,c, respectively. In Case 1, the void thickness and length are 15 and

243 mm, respectively. In Case 2, the void thickness and length are 15 and 186 mm, respectively. All field tests were completed under the same test conditions, with consistent transducer arrangement, excitation parameters, and signal preprocessing methods to ensure the consistency of the test results.

4.2 Experimental Signal Processing

Based on the sources and characteristics of noise and interference signals encountered during the actual detection process, a series of signal preprocessing methods have been proposed. These methods primarily include: removing the direct current (DC) component, eliminating surface waves, and performing noise reduction treatment. These measures can effectively support the reliability of subsequent imaging analysis and have been verified in prior researches [19,36].

(1) Removal of DC component

In actual received signals, there often exist a certain DC component, as illustrated in Fig. 13a. To eliminate the DC component from the received signal, a mean filtering process is applied to each column of data $A_i\ (i = 1, 2, 3 \ldots, N)$ according to Eq. (23). The signal after the removal of the DC component is shown in Fig. 13b.

$$A_i'(j) = A_i(j) - \frac{1}{M}\sum_{k=1}^{M} A_i(k),\ j = 1, 2, \ldots, N \tag{23}$$

where $A_i(j)$ and $A_i'(j)$ represent the original data and the data after the removal of the DC component for the j-th row of the i-th column, respectively. N denotes the number of columns in the matrix, and m denotes the number of rows in the matrix.

(2) Remove surface waves

According to the temporal characteristics of surface waves, the influence of surface waves can be mitigated by applying a window function to the detection signal. The specific method is as follows:

First, calculate the sound speed C_r of surface waves in concrete using Eq. (24).

$$C_\mathrm{r} = \frac{0.87 + 1.12\mu}{1 + \mu}\sqrt{\frac{E}{\rho}\left(\frac{1}{2(1+\mu)}\right)} \tag{24}$$

where μ represents the Poisson's ratio of the material, ρ denotes the material density, and E is the Young's modulus of the material.

Second, calculate the travel time t_1 of the surface wave signal from the position (x_i, y_i) of the excitation sensor to the position (x_j, y_j) of the receiving sensor using Eq. (25).

$$t_1 = \sqrt{\frac{(x_i - x_j)^2 + (y_i - y_j)^2}{C_r}} \tag{25}$$

Third, apply a window function to the detection signal in accordance with the rules specified in Eq. (26) to eliminate the surface wave signal.

$$S_{ij}^1 = \begin{cases} \delta S_{ij}(t), & 0 \le t \le t_2 \\ S_{ij}(t), & t > t_2 \end{cases} \tag{26}$$

where S_{ij}^1 represents the signal after the removal of the surface wave, $S_{ij}(t)$ denotes the original detection signal, δ is the suppression coefficient, t_1 and t_2 are the starting time and cut-off time of the surface wave,

respectively. If t_0 is the time width of the surface wave pulse, then it can be inferred that $t_2 = t_1 + t_0$. The signal after the removal of the surface wave is illustrated in Fig. 13c.

After the surface waves are removed using a window function, as recorded in reference [36], a smooth transition function is adopted to avoid discontinuity issues caused by the abrupt application of the window. However, this method may cause amplitude fluctuations in scattered signals.

(3) Suppress noise

To further reduce noise, filtering of the signal is necessary. However, different filtering methods yield different results, as demonstrated in existing literature. For example, the Chebyshev filter used in reference [19] enables accurate frequency selection but may cause waveform distortion. In reference [36], Gaussian smoothing filtering is employed, which can smooth the signal to reduce high-frequency noise without introducing phase distortion, but it cannot effectively target narrowband interference in specific frequency bands. In this paper, an elliptic filter is selected to maximize the preservation of the effective signal, minimize amplitude distortion, and simultaneously suppress noise. The filtered signal is shown in Fig. 13d. In comparison with Fig. 13c, it can be observed that this method effectively removes noise interference from the signal, resulting in a significant enhancement of the SNR.

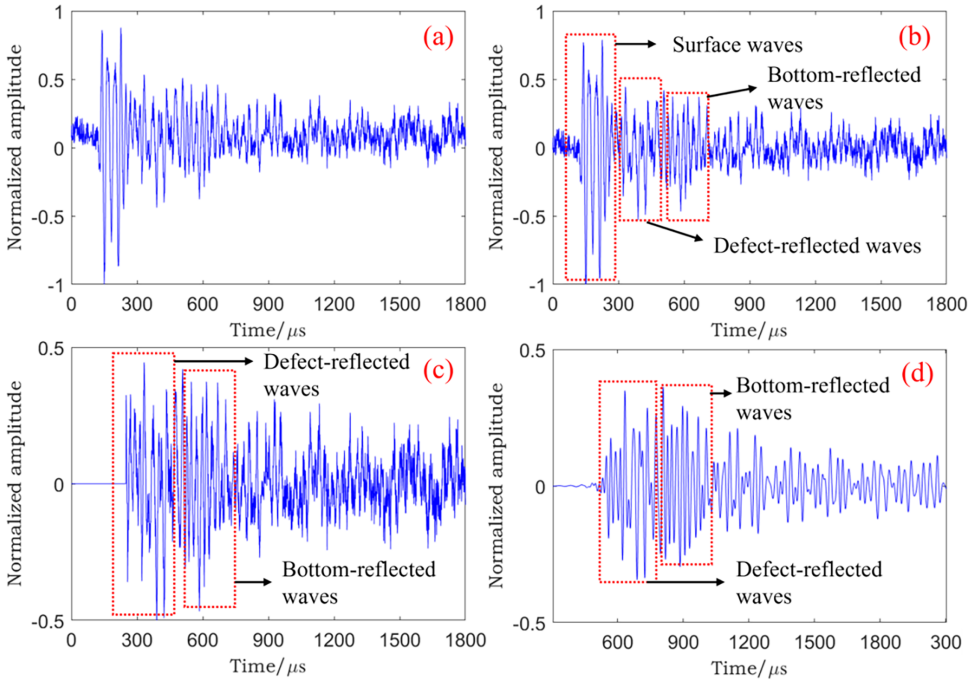

Figure 13: The processing process of experimental signal: (**a**) Original signal; (**b**) The signal after removing the DC component; (**c**) The signal after surface wave removal; (**d**) Filtered signal.

4.3 Experimental Results

(1) Analysis of imaging results for Case 1

The imaging of experimental signals for Case 1 was conducted using TFM, SPRT, PSPRT, and PPSPRT, with the results presented in Fig. 14. To facilitate a quantitative analysis of the imaging performance of the various methods, the transverse and longitudinal intensity curves of the ultrasonic images were extracted, as shown in Fig. 15, respectively, to assess the accuracy of defect localization. Additionally, the SNR of the images was computed to evaluate the effectiveness of noise suppression.

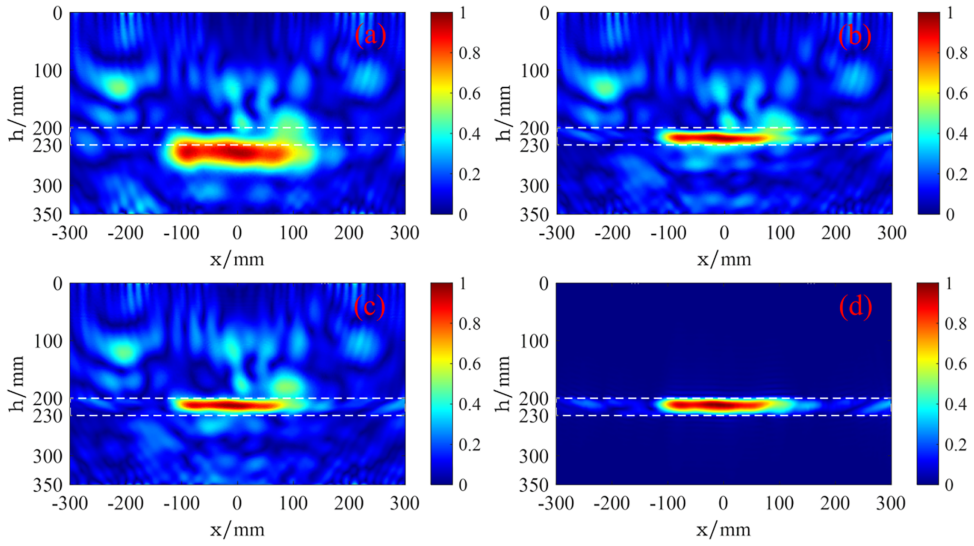

Figure 14: Experimental imaging results of Case 1: (**a**) TFM; (**b**) SPRT; (**c**) PSPRT; (**d**) PPSPRT.

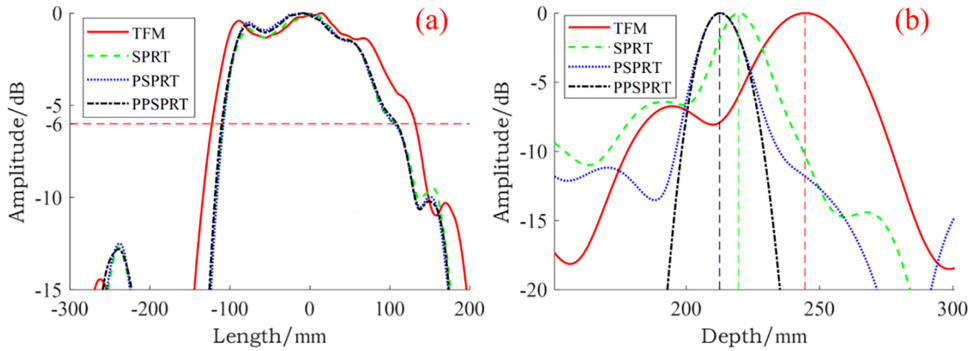

Figure 15: Experimental intensity curves of Case 1: (**a**) Transverse intensity curves; (**b**) Longitudinal intensity curves.

From the ultrasonic images, it can be observed that TFM effectively detects the void defect; however, it exhibits severe artifacts surrounding the defect, making it challenging to accurately determine the defect's size and depth. Moreover, the image SNR is low, resulting in poor imaging quality. SPRT mitigates the artifacts around the defect and allows for assessment of the defect size; however, it similarly suffers from low image SNR and poor quality, with discrepancies in the localization of the defect depth. With the added correction for acoustic time through the pulse peak delay term, PSPRT provides more accurate defect localization, though noise interference still persists around the defect. PPSPRT not only effectively suppresses artifacts surrounding the defect, significantly enhances the image SNR, but also provides precise localization of the defect.

(2) Analysis of imaging results for Case 2

The imaging of experimental signals for Case 2 was conducted using TFM, SPRT, PSPRT, and PPSPRT, with the results presented in Fig. 16. To facilitate a quantitative analysis of the imaging performance of the various methods, the transverse and longitudinal intensity curves of the ultrasonic images were extracted, as shown in Fig. 17, respectively, to evaluate the accuracy of defect localization. Additionally, the SNR of the images was computed to assess the effectiveness of noise suppression.

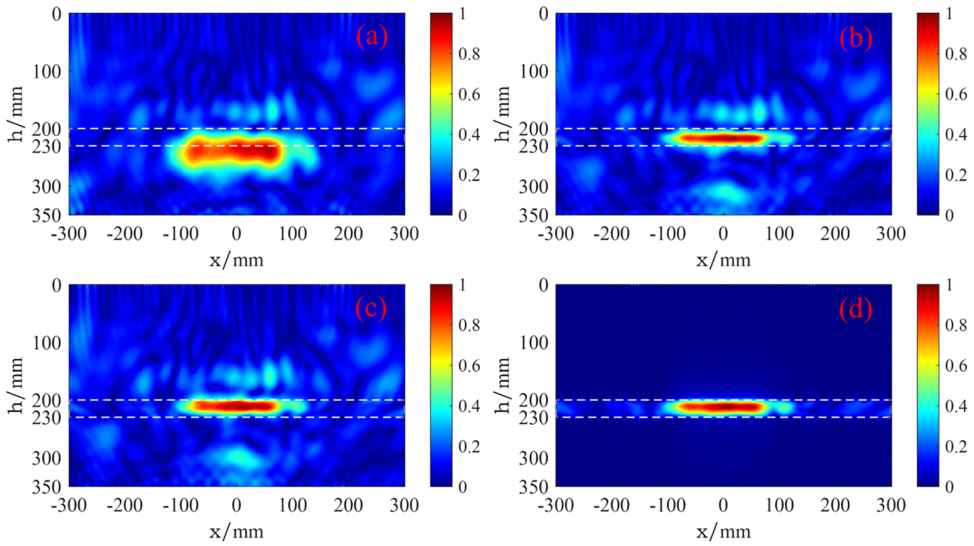

Figure 16: Experimental imaging results of Case 2: (**a**) TFM; (**b**) SPRT; (**c**) PSPRT; (**d**) PPSPRT.

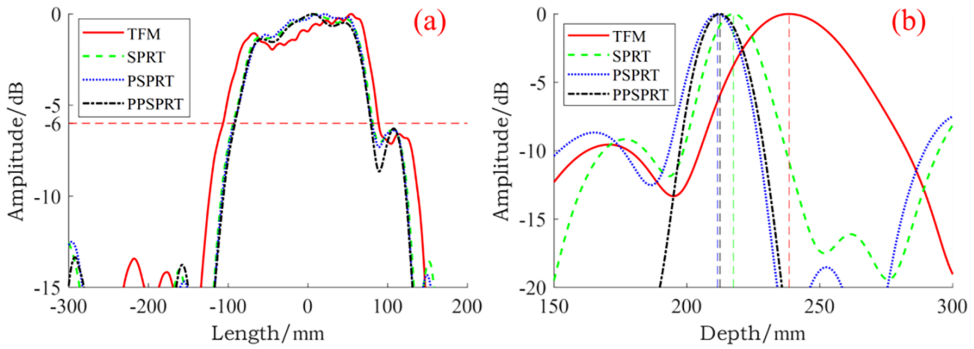

Figure 17: Experimental intensity curves of Case 2: (**a**) Transverse intensity curves; (**b**) Longitudinal intensity curves.

Based on the ultrasonic images presented in Figs. 14 and 16, the SNR for the four ultrasonic imaging methods—TFM, SPRT, PSPRT, and PPSPRT—were calculated for Case 1 and Case 2, as summarized in Table 5. In the defect detection experiment for Case 1, PPSPRT achieved improvements in SNR of 15.04, 13.17, and 13.40 dB compared to TFM, SPRT, and PSPRT, respectively. In the defect detection experiment for Case 2, PPSPRT enhanced SNR by 13.57, 12.02, and 12.48 dB over TFM, SPRT, and PSPRT, respectively. It is evident that PPSPRT effectively suppresses artifacts in the ultrasonic images, resulting in a significant improvement in image SNR. Compared with TFM, PPSPRT achieves an average SNR improvement of 14.30 dB in the two test cases.

Table 5: SNR of ultrasound images obtained from experiments (unit: dB).

Method	Case 1	Case 2	Average SNR
TFM	15.16	16.55	15.86
SPRT	17.03	18.10	17.57
PSPRT	16.80	17.64	17.22
PPSPRT	30.20	30.12	30.16

According to the ultrasonic imaging intensity curves shown in Figs. 15 and 17, the lengths and depths of the void defects have been calculated, as detailed in Table 6. The research findings indicate that:

(1) Regarding depth localization of the voids, TFM is capable of detecting void defects; however, the average depth error derived from TFM reaches approximately 26.5 mm in the two test cases. In contrast, the SPRT, the PSPRT, and the PPSPRT demonstrate higher accuracy in depth localization. Notably, the average depth localization error for PPSPRT is approximately 2.75 mm in the two test cases.

(2) In terms of void length assessment, all four methods are able to differentiate between void defects of varying lengths. While the void length obtained through TFM is closer to the actual length, there is a significant discrepancy between the defect position indicated by this method and the true position. Therefore, TFM exhibits considerable limitations in imaging accuracy. Conversely, SPRT, PSPRT, and PPSPRT yield results that are more aligned in void length detection.

Table 6: Evaluation of void length and depth based on experimental results (unit: mm).

Case	Parameters in Detected	TFM	SPRT	PSPRT	PPSPRT
Case 1	Detected length	254	216	212	218
	Length error	11	27	31	25
	Detected depth	244.5	219.5	212	212
	Depth error	29.5	4.5	3	3
Case 2	Detected length	195	175.5	173	170
	Length error	9	10.5	13	16
	Detected depth	238.5	217.5	211.5	212.5
	Depth error	23.5	2.5	3.5	2.5
Average error	Average length error	10	18.75	22	20.5
	Average depth error	26.5	3.5	3.25	2.75

5 Discussion

5.1 The SNR of Ultrasonic Images

Under the premise that the void thickness is uniformly 15 mm and the void depth is consistently 215 mm, ultrasonic imaging detection was conducted using TFM, SPRT, PSPRT, and PPSPRT for voids measuring 300, 250, 200, and 150 mm in length. The ultrasonic images are presented in Figs. 10 and 18–20, respectively. The SNR and their averages for the simulated images obtained using different methods at varying void lengths are summarized in Table 7. The research findings indicate that:

(1) In terms of SNR, a sequential enhancement is observed from TFM to SPRT, PSPRT, and ultimately to PPSPRT. Compared with TFM, PPSPRT achieves an average SNR improvement of 6.62 dB across all simulated void sizes. This enhancement is attributed to the fact that PPSPRT adequately incorporates the amplitude and phase information of low-frequency ultrasonic signals and accounts for wave delay corrections, resulting in higher image SNR.

(2) As the length of the voids decreases, the SNR of ultrasonic images produced by all methods increases. This improvement can be explained by the fact that with smaller horizontal void lengths, the deflection angle of the acoustic waves reaching the void's end surface diminishes. Given that low-frequency ultrasound exhibits poorer directivity, the energy of defect echoes at small angles is comparatively stronger than that of echoes at larger angles, leading to superior detection performance for shorter void lengths.

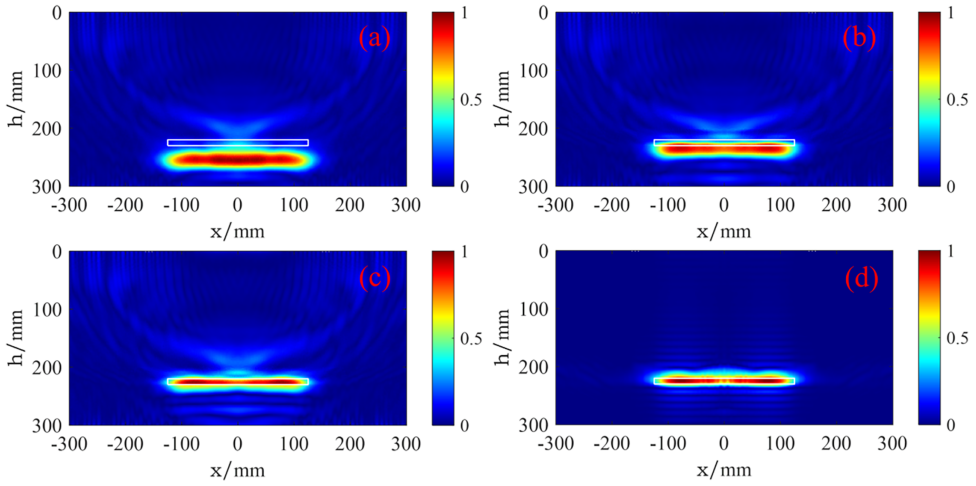

Figure 18: Numerical imaging results of different methods (the length of void is 250 mm): (**a**) TFM; (**b**) SPRT; (**c**) PSPRT; (**d**) PPSPRT.

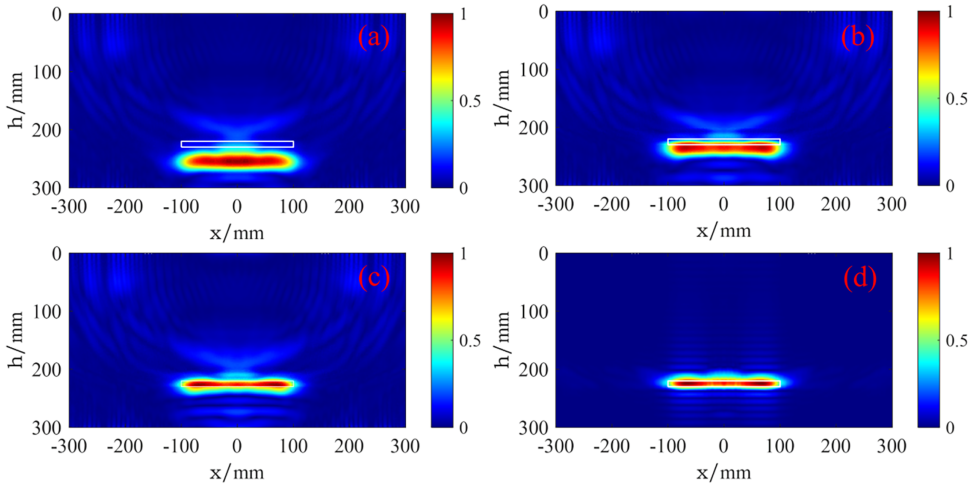

Figure 19: Numerical imaging results of different methods (the length of void is 200 mm): (**a**) TFM; (**b**) SPRT; (**c**) PSPRT; (**d**) PPSPRT.

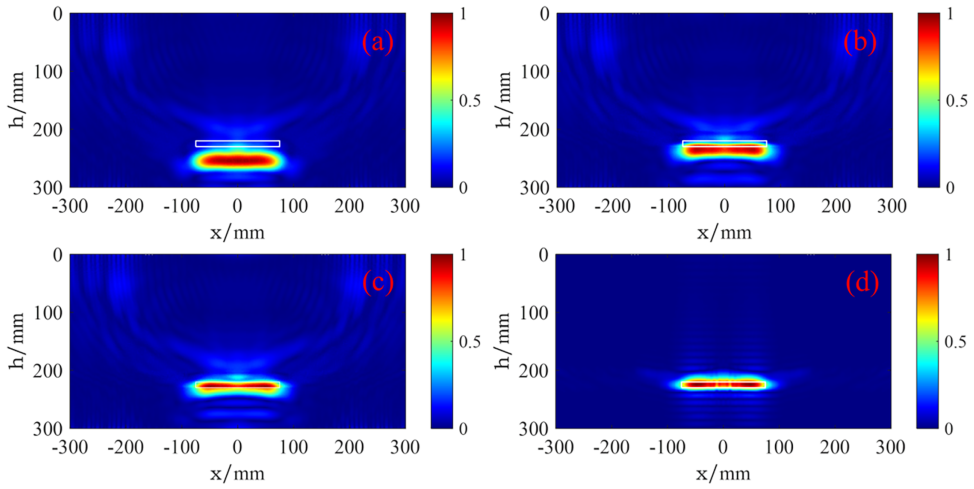

Figure 20: Numerical imaging results of different methods (the length of void is 150 mm): (**a**) TFM; (**b**) SPRT; (**c**) PSPRT; (**d**) PPSPRT.

Table 7: SNR of numerical images under different lengths of voids (unit: dB).

Method	300 mm	250 mm	200 mm	150 mm	Average SNR
TFM	21.42	22.56	24.02	25.99	23.50
SPRT	22.14	23.55	24.45	26.19	24.08
PSPRT	22.38	23.63	24.74	26.45	24.30
PPSPRT	27.88	29.12	30.73	32.75	30.12

In summary, the TFM fails to account for differences in sound speed across various media, leading to a certain degree of positional deviation for the void defects in the imaging results, as well as an increased presence of noise that adversely affects image quality. In contrast, the SPRT calculates a more accurate sound transit time based on acoustic wave velocities in different media, resulting in detected void defect positions that are closer to their actual locations; however, some deviation persists, and noise issues remain prominent. The PSPRT incorporates a delay peak adjustment to correct the sound transit times, thus bringing the detected defect positions closer to actual values, yet the images still contain considerable noise. When utilizing the PPSPRT for defect detection, it is observed that not only is the positional deviation of the defects in the ultrasonic images significantly reduced, but the image noise is also markedly diminished.

5.2 Evaluation of Interlayer Voids in Length and Depth

The intensity curves extracted from void images with lengths of 300, 250, 200, and 150 mm are illustrated in Figs. 11 and 21–23. The simulated void lengths and depths are evaluated as shown in Table 8. The findings indicate that: (1) as the void length decreases, the detection errors for void length across all methods tend to decrease, while the detection errors for void depth remain relatively constant; (2) the average depth error for the TFM is approximately 39.38 mm, whereas the average depth error for the PPSPRT method is only about 9.25 mm. The average depth localization error of voids for the PPSPRT method is only approximately 23.49% of that for the TFM method (calculated as $9.25/39.38 \times 100\% \approx 23.49\%$). This confirms that for low-frequency ultrasonic detection, performing sound time correction and phase coherence calculations is crucial for accurately locating defect depths. (3) TFM exhibits high accuracy in void length detection, with

an average error of approximately 3.75 mm. However, due to TFM's significant errors in depth localization, its overall performance in size assessment is suboptimal.

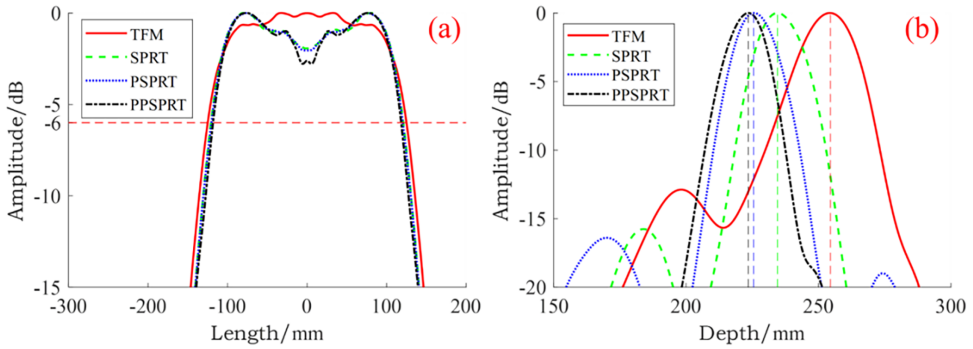

Figure 21: Numerical intensity curves of different methods (the length of void is 250 mm): (**a**) Transverse intensity curves; (**b**) Longitudinal intensity curves.

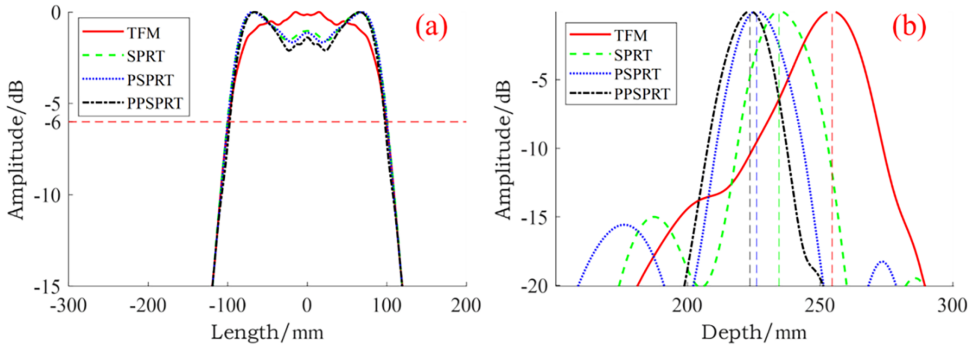

Figure 22: Numerical intensity curves of different methods (the length of void is 200 mm): (**a**) Transverse intensity curves; (**b**) Longitudinal intensity curves.

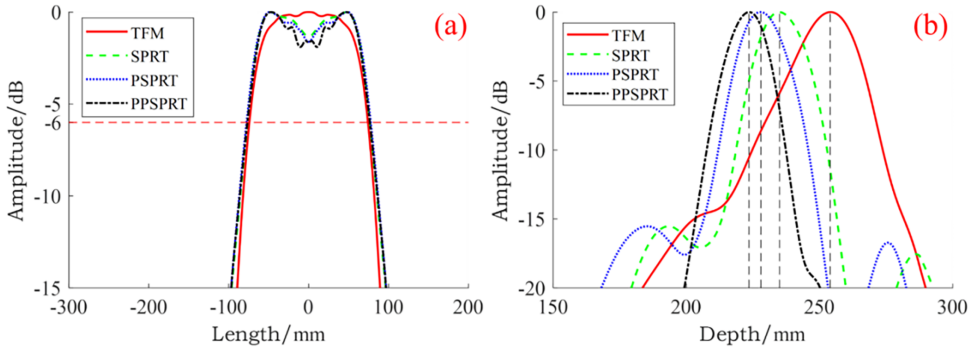

Figure 23: Numerical intensity curves of different methods (the length of void is 150 mm): (**a**) Transverse intensity curves; (**b**) Longitudinal intensity curves.

Table 8: Evaluation of length and depth based on numerical results (unit: mm).

Actual Value	Detected Value	TFM	SPRT	PSPRT	PPSPRT
300 in length	Detected length	289	281	280	278
	Length error	11	19	20	22
215 in depth	Detected depth	254.5	235	227.5	224.5
	Depth error	39.5	20	12.5	9.5
250 in length	Detected length	250	242	241	237
	Length error	0	8	9	13
215 in depth	Detected depth	254.5	234.5	225.5	224.5
	Depth error	39.5	19.5	10.5	9.5
200 in length	Detected length	198	201	201	195
	Length error	2	1	1	5
215 in depth	Detected depth	254.5	234.5	226	224.5
	Depth error	39.5	19.5	11	9.5
150 in length	Detected length	148	153	156	153
	Length error	2	3	6	3
215 in depth	Detected depth	254	235	228	223.5
	Depth error	39	20	13	8.5
Average error	Average length error	3.75	7.75	9.00	10.75
	Average depth error	39.38	19.75	11.75	9.25

5.3 Influence of Void Length on the Imaging Performance of PPSPRT

As demonstrated in the preceding sections, PPSPRT exhibits superior performance in terms of SNR and depth localization accuracy when detecting voids of various lengths, compared to TFM, SPRT, and PSPRT. However, it is worth noting that although PPSPRT significantly improves depth localization accuracy and SNR, it does not outperform other methods in all metrics. As shown in Table 8, the average length error of the conventional TFM is only 3.75 mm, which is considerably smaller than that of PPSPRT (10.75 mm) and the other proposed methods. TFM, which relies on a single velocity model, tends to produce images where the horizontal span of the defects is relatively well preserved, albeit at the cost of substantial depth errors and pronounced artifacts. In contrast, PPSPRT enhances depth localization and suppresses noise through phase coherence and accurate ray tracing, which leads to an underestimation of the defect length. This phenomenon can be attributed to the phase coherence factor: while it effectively suppresses sidelobes and artifacts, it may also attenuate scattered signals originating from the edges of the void, thereby slightly reducing the perceived horizontal extent. Although the PPSPRT's estimation of defect length is slightly less accurate, this trade-off has led to a significant improvement in depth positioning accuracy and SNR.

Based on the data in Table 8, the lateral length detection error of the PPSPRT method decreases significantly as the void length reduces: when the void length decreases from 300 to 150 mm, the absolute error drops from 22 to 3 mm, indicating that the smaller the defect size, the higher the length detection accuracy. This phenomenon is closely related to the effective detection aperture of the array. The effective aperture of the 12-element linear array used in this study (with an element pitch of 30 mm) is 330 mm.

When the defect size is comparable to this aperture, the scattered echoes from the edge regions at both ends can only be received by a few elements at the extremities of the array, resulting in insufficient data. Moreover, large-angle scattered waves from the defect edges suffer severe attenuation after refraction through multilayer interfaces, significantly reducing both the SNR and phase coherence. The SCF employed in PPSPRT further suppresses these weakly coherent signals, weakening the imaging response at the defect edges and leading to a larger length detection error for large-scale voids comparable to the array aperture. Conversely, when the defect size is significantly smaller than the array aperture, most elements can receive strongly coherent scattered signals. In this case, the suppression effect of SCF on the defect edge is reduced, thus significantly improving the transverse length detection accuracy.

In conclusion, while PPSPRT has some limitations in accurately estimating the lateral size of defects, particularly for large voids near the effective aperture of the array, this trade-off is accompanied by a significant enhancement in depth positioning accuracy and SNR. Additionally, the improvement in the detection accuracy of smaller defects further demonstrates the effectiveness of PPSPRT for identifying small-sized defects. Future work will focus on integrating complementary indicators or hybrid methods to preserve the strengths of PPSPRT while addressing its tendency to underestimate lateral size, ultimately achieving a more balanced and robust performance across a range of detection scenarios.

5.4 Influence Analysis of Complex Situations

The preliminary numerical simulation in this study was established based on the material assumption of homogeneous plain concrete. Whereas in practical high-speed railway ballastless track engineering, both the track slab and base slab are reinforced concrete structures containing randomly distributed aggregates and steel bar. The multi-interface scattering induced by aggregates and the reflection from steel bars will introduce extra clutter interference, which may exert an impact on ultrasonic imaging performance. Accordingly, this section additionally establishes a concrete model incorporating random aggregates and steel bar, and carries out a comparative analysis against the homogeneous plain concrete benchmark model. All models used in this section follow the three-layer ballastless track structure specified in Section 3.1. The schematic diagram of the established models is presented in the Fig. 24, and the material parameters of the aggregates and steel bars are tabulated in the Table 9. In Fig. 24b, the blue markings represent steel bars, and the black markings represent aggregates.

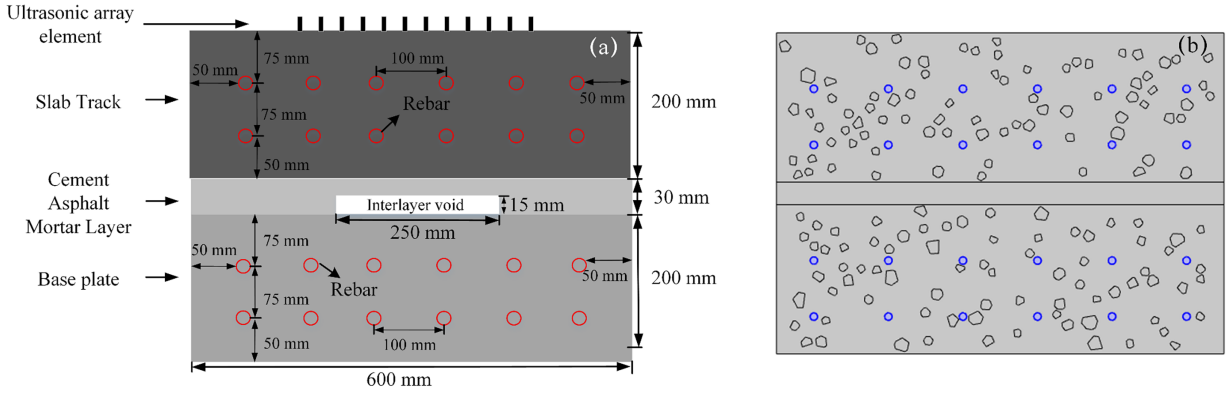

Figure 24: Finite element simulation model: (**a**) schematic diagram of the model; (**b**) model created using Comsol.

Table 9: Parameters of aggregates and reinforcing bars.

Material	Density (kg/m^3)	Poisson's Ratio	Elastic Modulus (GPa)	Diameter Size (mm)	Shape
Aggregate	2700	0.25	60	7~12	Polygon
Steel	7850	0.3	205	10	Circle

The imaging results of the two types of concrete models using the PPSPRT algorithm are shown in Fig. 25. Among them, the SNR of the imaging result of the heterogeneous concrete model containing aggregates and steel bars is 27.51 dB, and the SNR of the imaging result of the homogeneous plain concrete benchmark model is 29.12 dB. It can be seen from the imaging results that the interlayer void shown in Fig. 25a has non-smooth characteristics, which is caused by the clutter interference introduced by the interface scattering of aggregates and the reflection of steel bars inside the concrete. Compared with the imaging results of the homogeneous plain concrete benchmark model, although the imaging quality of the heterogeneous concrete model has a slight decrease, there is no significant difference in the core identification and positioning effect of interlayer voids between the two models. Therefore, all simulation analyses recorded in this paper are carried out with the homogeneous plain concrete model.

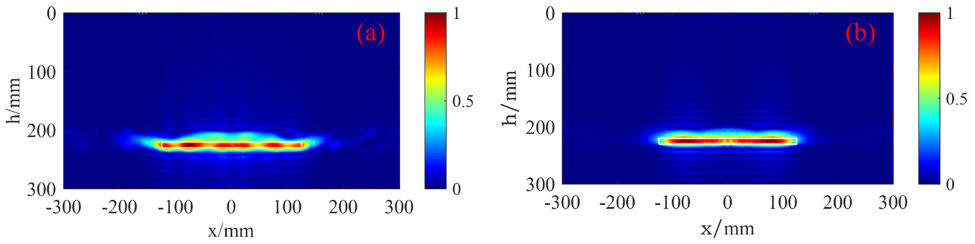

Figure 25: Numerical imaging results of different models: (**a**) Non-uniform concrete; (**b**) Uniform concrete.

Additionally, this study focuses on the most typical engineering scenario of interlayer voids in high-speed railway ballastless tracks, and simplifies the void region as an air-filled cavity model, with the core objective of verifying the fundamental performance of the proposed algorithm in the detection, localization and imaging of interlayer voids. In practical engineering, void defects are accompanied by complex working conditions such as irregular geometry, partial interface contact, debris filling and moisture ingress. Although the above factors do not alter the significant acoustic impedance contrast between the void region and the concrete matrix, they may still cause certain interference to the quantitative detection accuracy of defect dimensions. Subsequent research will systematically analyze the influence law of various complex working conditions on the algorithm performance, to further optimize its engineering adaptability.

5.5 Influence Analysis of Phase Weighting Methods

To clarify the rationality of selecting the SCF in this paper, this section supplements the comparative analysis of the imaging performance of three phase weighting methods: SCF, Phase Coherence Factor (PCF), and Circular Coherence Factor (CCF). All comparative tests are based on the identical simulation data, hardware environment and imaging grid parameters in Section 3.1 of this paper, and the test results are shown in Table 10 and Fig. 26. It can be seen from the comparison results that although the imaging results weighted by PCF are slightly higher than SCF in SNR, they have serious distortion in the reconstruction of defect morphology, and the imaging time consumption is significantly higher than SCF; in addition, compared with

the CCF weighting scheme, SCF has obvious advantages in both imaging SNR and reconstruction accuracy of defect morphology. Therefore, after comprehensive consideration, SCF is finally selected as the phase weighting scheme in this paper, which is more suitable for the engineering detection scenario of interlayer voids in ballastless tracks.

Table 10: Performance comparison of different methods.

Phase Weighting Method	SNR (dB)	Required Imaging Time (s)
SCF	29.12	36.601
PCF	32.16	45.857
CCF	22.51	36.144

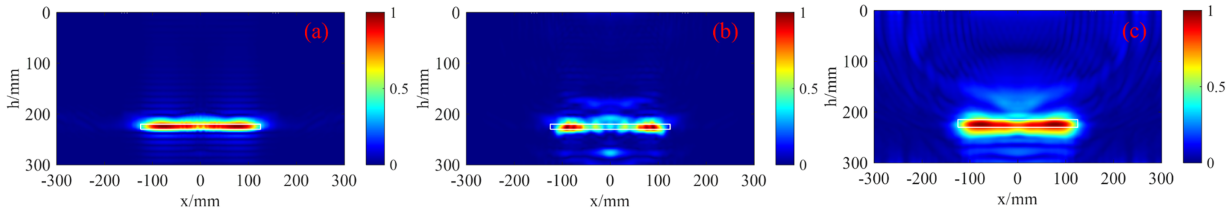

Figure 26: Numerical imaging results of different methods (the length of void is 250 mm): (**a**) SCF; (**b**) PCF; (**c**) CCF.

6 Conclusion

To address the challenges of inaccurate localization and low SNR in ultrasonic testing for interlayer voids in multilayer ballastless track structures, The PPSPRT imaging method based on low-frequency ultrasonic arrays has been conducted. The specific content is as follows:

(1) Based on *Fermat's* principle and *Snell's* law, the SPRT method is proposed, which imposes dual constraints on the position and search range of refraction points. It reduces the computational time for void imaging in multilayer structures by 26.1% relative to the traditional MTRT method, markedly enhancing imaging efficiency.

(2) Based on the SPRT method, the PPD factor is incorporated to establish the PSPRT method for correcting the travel time of low-frequency ultrasound. Simulation and experimental results validate that this method markedly enhances the accuracy of defect depth localization.

(3) The proposed PPSPRT method is developed by integrating the amplitude and phase characteristics of scattered signals, which effectively suppresses imaging artifacts and significantly improves the accuracy of defect depth localization. Compared with the conventional TFM, PPSPRT achieves an average SNR improvement of 6.62 and 14.30 dB in numerical simulation and field tests, respectively; meanwhile, the average depth localization error of interlayer voids yielded by PPSPRT is only approximately 23.49% and 10.38% of that obtained with TFM under the corresponding simulation and experimental conditions, respectively.

Although the proposed PPSPRT has enhanced the imaging accuracy for defects in multilayer concrete structures, there are still shortcomings. Future research will be pursued in the following areas:

(1) Considering that the sound field generated by the ultrasonic transducer has a spatial distribution characteristic, future work will focus on optimizing the beamforming algorithm and correcting the radiated energy of the acoustic waves in space, thereby enhancing the capability to detect defects at large angles.

(2) Recognizing that two-dimensional imaging may not comprehensively reflect the spatial distribution and morphological characteristics of defects, future studies will investigate three-dimensional real-time ultrasonic imaging, aiming to improve detection precision and applicability.
(3) Considering the random distribution of aggregates in concrete, the spatial distribution of reinforcing bars in the structure, the irregular morphological characteristics of voids, and the diverse filling media within defects, the future study will systematically evaluate the impacts of these factors on the imaging process to further enhance the engineering robustness of the proposed method under complex field application scenarios.

Acknowledgement: None.

Funding Statement: The work was supported by the National Natural Science Foundation of China (Grant No. 12304514).

Author Contributions: Guopeng Fan: Investigation, Methodology, Software, Validation, Writing—original draft, Funding acquisition. Xuefeng Chen: Data curation, Software, Validation. Hao Liu: Software, Validation, Formal analysis. Jiaqing Zheng: Conceptualization, Visualization. All authors reviewed and approved the final version of the manuscript.

Availability of Data and Materials: Data will be made available on request.

Ethics Approval: Not applicable.

Conflicts of Interest: The authors declare no conflicts of interest.

References

1. Guo W, Ye Y, Hu Y. Seismic damage analysis of bridge-CRTS III slab ballastless track system on high-speed railway. Soil Dyn Earthq Eng. 2022;161:107416. doi:10.1016/j.soildyn.2022.107416.
2. Guo G, Hao C, Du B. Static and dynamic response characteristics of a ballastless track structure of a high-speed railway bridge with interlayer debonding under temperature loads. Eng Fail Anal. 2023;151:107377. doi:10.1016/j.engfailanal.2023.107377.
3. Hu M, Xu Y, Xue Z, Wang S. An inversion method for evaluating ballastless track degradation based on multi-channel analysis of surface wave. Mech Syst Signal Process. 2023;200:110572. doi:10.1016/j.ymssp.2023.110572.
4. Zhu WF, Chen XJ, Li ZW, Meng XZ, Fan GP, Shao W, et al. A SAFT method for the detection of void defect inside a ballastless track structure using ultrasonic array sensors. Sensors. 2019;19(21):4677. doi:10.3390/s19214677.
5. Dong H, Li H, Shi H, Wen J, Wang Z, Huang F, et al. Evaluation index and improvement method for interlayer bonding property of ballastless track. Eng Fail Anal. 2023;153:107620. doi:10.1016/j.engfailanal.2023.107620.
6. Shi T, Lou P. Optimized machine learning approaches for identifying vertical temperature gradient on ballastless track in natural environments. Constr Build Mater. 2023;367:130321. doi:10.1016/j.conbuildmat.2023.130321.
7. Zhang X, Wang L, Tang S, Cui H, Xie X, Wu H, et al. Investigations on the shearing performance of ballastless CRTS II slab based on quasi-distributed optical fiber sensing. Opt Fiber Technol. 2023;75:103129. doi:10.1016/j.yofte.2022.103129.
8. Chen X, Pei Y, Liu K. Dynamic response of train-ballastless track caused by failure in cement-asphalt mortar layer. Buildings. 2025;15(3):334. doi:10.3390/buildings15030334.
9. Wang J, Lu ZH, Li CQ. A novel mixed-mode interface damage model based on exponential traction-separation law. Constr Build Mater. 2025;490:142454. doi:10.1016/j.conbuildmat.2025.142454.
10. Jin H, Wu E, Han Y, Yang K, Chen J. Frequency domain synthetic aperture focusing technique for variable-diameter cylindrical components. J Acoust Soc Am. 2017;142(3):1554. doi:10.1121/1.5003650.
11. Yan X, Fan G, Zhu W, Zhang H, Chai X, Xie X, et al. High-resolution ultrasonic image reconstruction of shallow rail defects using a relativistic-attention-weighted CycleGAN. Nondestruct Test Eval. 2025;32:1–29. doi:10.1080/10589759.2025.2541051.

12. Tian J, Chen Z, Lu S, Qi X, Pu S, Liu M. Phase coherence weighted ultrasound total focusing method towards the improved imaging of CFRP defects. Compos Commun. 2023;43:101736. doi:10.1016/j.coco.2023.101736.
13. Lu M, Zhu K, Wang Q. Fatigue crack detection in steel plates using guided waves and an energy-based imaging approach. Struct Durab Health Monit. 2021;15(3):207–25. doi:10.32604/sdhm.2021.017720.
14. Ying KN, Ni CY, Dai LN, Cao WX, Yang Z, Yuan L, et al. Multi-iteration frequency-domain synthetic aperture focusing technique (MIF-SAFT) in multi-mode laser ultrasound for image quality improvement. Mech Syst Signal Process. 2024;216:111478. doi:10.1016/j.ymssp.2024.111478.
15. Wang C, Wang K, Zhu J, Dong D, Chang J. Ultrasound imaging of bottom opening crack based on frequency-domain reverse time migration. IEEE Access. 2022;10:68202–12. doi:10.1109/ACCESS.2022.3186302.
16. Brizuela J, Camacho J, Cosarinsky G, Iriarte JM, Cruza JF. Improving elevation resolution in phased-array inspections for NDT. NDT E Int. 2019;101:1–16. doi:10.1016/j.ndteint.2018.09.002.
17. Fan G. Non-destructive testing of internal cracks in concrete using low-frequency ultrasonic array frequency wavenumber domain method combined with pulse peak delay factor. AIP Adv. 2025;15(8):085108. doi:10.1063/5.0268669.
18. Li F, Di SK, Zhang J, Yang D, Pei Y, Wang XY. Detection of internal defects in concrete using delay multiply and sum-enhanced synthetic aperture focusing technique. Buildings. 2025;15(11):1887. doi:10.3390/buildings15111887.
19. Yang J, Fan G, Xiang Y, Zhang H, Zhu W, Zhang H, et al. Low-frequency ultrasonic array imaging for detecting concrete structural defects in blind zones. Constr Build Mater. 2024;425:135948. doi:10.1016/j.conbuildmat.2024.135948.
20. Zhang L, Qiao C, Jia S, Zeng J, Li H, Zhang T, et al. Imaging of inclusions in concrete with enhanced low-frequency ultrasound tomography. Sens Actuat A Phys. 2025;386:116324. doi:10.1016/j.sna.2025.116324.
21. Zhan H, Jiang H, Jiang R. Three-dimensional images generated from diffuse ultrasound wave: detections of multiple cracks in concrete structures. Struct Health Monit. 2020;19(1):12–25. doi:10.1177/1475921719834045.
22. Yang Z, Kong Q, Chen L. High-resolution imaging of concrete cracks using a time reversal-based method. Int J Mech Sci. 2025;307:110942. doi:10.1016/j.ijmecsci.2025.110942.
23. Baek S, Jeon S, Kim J, Joo YS, Kim C, Hwang YH, et al. Exploring the potential of null subtraction imaging for detecting sub-rebar regions in reinforced concrete structures at nuclear power plants. Nondestruct Test Eval. 2025:1–16. doi:10.1080/10589759.2025.2505086.
24. Dolmatov DO. Method for calculating the point spread function for the ultrasonic imaging of multi-layered objects with total focusing method. Russ Phys J. 2025;68(3):540–8. doi:10.1007/s11182-025-03462-8.
25. Zhang J, Drinkwater BW, Wilcox PD, Hunter AJ. Defect detection using ultrasonic arrays: the multi-mode total focusing method. NDT E Int. 2010;43(2):123–33. doi:10.1016/j.ndteint.2009.10.001.
26. Holmes C, Drinkwater BW, Wilcox PD. Post-processing of the full matrix of ultrasonic transmit-receive array data for non-destructive evaluation. NDT E Int. 2005;38(8):701–11. doi:10.1016/j.ndteint.2005.04.002.
27. Budyn N, Bevan RL, Zhang J, Croxford AJ, Wilcox PD. A model for multiview ultrasonic array inspection of small two-dimensional defects. IEEE Trans Ultrason Ferroelectr Freq Control. 2019;66(6):1129–39. doi:10.1109/tuffc.2019.2909988.
28. Wu Y, Wang Y, Li D, Zhang J. Two-step detection of concrete internal condition using array ultrasound and deep learning. NDT E Int. 2023;139:102945. doi:10.1016/j.ndteint.2023.102945.
29. Lin S, Shams S, Choi H, Azari H. Ultrasonic imaging of multi-layer concrete structures. NDT E Int. 2018;98:101–9. doi:10.1016/j.ndteint.2018.04.012.
30. Zhu WF, Shao W, Peng LL, Fan GP, Chen XJ, Zheng SB, et al. Time-domain topological energy imaging method of concrete cavity defect by lamb wave. Shock Vib. 2019;2019(1):6294603. doi:10.1155/2019/6294603.
31. Li ZW, Zhu WF, Meng XZ, Fan GP, He YL. Multi-layer imaging method for void defects in ballastless track using forward ray tracing with SAFT. Measurement. 2021;173:108532. doi:10.1016/j.measurement.2020.108532.
32. Si J, Zhang H, Zhang H, Zhu W, Fan G, Chen Y, et al. Ultrasonic detection of adhesive quality behind tunnel lining with fast multi-layer ray tracing. J Civ Struct Health Monit. 2025;15(8):3801–18. doi:10.1007/s13349-025-01017-6.

33. Gantala T, Gurunathan MR, Balasubramaniam K. Arbitrary virtual array source aperture (AVASA) ultrasound imaging technique using phased array excitation. J Nondestruct Eval. 2023;42(3):71. doi:10.1007/s10921-023-00985-3.
34. Chen Y, Rong L, Song Y, Yang X. Detection of internal defects in concrete by ultrasonic total focusing imaging using the delay-multiply-and-sum method. KSCE J Civ Eng. 2025;29(7):100235. doi:10.1016/j.kscej.2025.100235.
35. Zimermann R, Mohseni E, Lines D, Vithanage RKW, MacLeod CN, Pierce SG, et al. Multi-layer ultrasonic imaging of as-built Wire + Arc additive manufactured components. Addit Manuf. 2021;48:102398. doi:10.1016/j.addma.2021.102398.
36. Sun Z, Yang L, Liu M, Ma Y, Li D. Adaptive amplitude-phase fusion based ultrasonic imaging for internal defect detection in precast concrete components. Mech Syst Signal Process. 2025;240:113377. doi:10.1016/j.ymssp.2025.113377.